MECHANISTIC MODELING OF BEARING PAD TO PRESSURE TUBE CONTACT UNDER LOCALIZED HIGH TEMPERATURE CONDITIONS IN A CANDU FUEL CHANNEL

FARSHAD TALEBI¹, JOHN C. LUXAT¹

¹ McMaster University, Hamilton, Ontario, Canada L8S 4L7 e-mail: farshat@mcmaster.ca, behdada@mcmaster.ca, luxatj@mcmaster.ca

ABSTRACT

During a postulated critical break LOCA (loss of coolant accident) in a CANDU reactor the coolant flow rates in the fuel channels of the flow pass of the reactor core downstream of the pipe break can rapidly reduce to very low values and remain very low for a period of tens of seconds following the break. Under the sustained low flow conditions, the fuel sheath (cladding) temperature in the affected channels rapidly increases and the coolant in the channels becomes significantly voided. The pressure tubes in the affected pass heat up under a combination of convection heat transfer from the low flows of superheated seam and thermal radiation heat transfer from the hot fuel. Additionally, hot spots may develop on the inner surface of pressure tubes at locations where the fuel bearing pads are in direct contact with the pressure tube. Localized thermal creep strain deformation at the hot spots is a potential pressure tube failure mechanism which could challenge fuel channel integrity. This paper evaluates the local thermalmechanical deformation of a pressure tube in a CANDU reactor under critical break LOCA conditions tube using a coupled thermal-mechanical finite element COMSOL multi-physics model and investigates the conditions resulting in fuel channel failure due to localized contact between bearing pad and pressure. The mechanistic models are validated against data obtained from COG funded experiments performed at WRL (Whiteshell Research Laboratory). Multiphysics calculations are performed in which the heat transfer, thermal-mechanical and creep strain equations are solved, simultaneously. Heat conduction from bearing pads to the inner surface of the pressure tube is modeled with appropriate convective and radiation heat transfer boundary conditions. Thermal creep strain deformation of the Zr-2.5%Nb pressure tube is modeled using correlations derived from separate uniaxial tests that are reported in the literature. Contact conductance models based on experimental correlation are employed to calculate heat conduction through contacting boundaries of the bearing pads and pressure tube. The results of the analysis establish that localized pressure tube thermal strain causing failure of the pressure tube requires both sufficiently high local temperatures and pressures, and also depends on the extent of steam cooling of the pressure tube away from the contact point between the bearing pads and pressure tube in the fuel channel. Parametric analysis is presented that evaluates the sensitivity of pressure tube local strain to modeling the contact conductance, contact width and zircaloy surface emissivity.

Keyword: Thermal creep strain, Mechanical deformation, CANDU reactor, Local hot spots, Bearing pad to pressure tube contact, Contact conductance.

1. INTRODUCTION

Normally, the fuel elements (FEs) are not in direct contact with the pressure tube (PT) except at the bearing pads (BPs) of the outer elements at the bottom of the bundle. During a postulated LOCA with failure of ECIS, if the pressure tube temperature increases and coolant flow sufficiently degrades in the fuel channel, the influence of hot bearing pads on the pressure tube temperature transient and the consequence of mechanical deformation is very important to be studied. Therefore, twelve series of BPs to PT contact experiments have been performed at WRL under CANDU Owner Group (COG).[1-4] The main differences considered in the experimental conditions were pressurizing medium, pressure tube internal pressure, bearing pad types and test section power. An interesting result was obtained in the fifth series of experiments, where the sides and bottom of the pressure tube were hotter than the top during the high power heatup phase resulting in significant preferential wall thinning ($\sim 68\%$) directly under the bottom bearing pad during ballooning contact. This was the starting point of the present research, where we have attempted to evaluate the effect of BPs to PT contact behavior under same condition using the COMSOL software package^[5] and validate the results against the fifth test. Therefore, the validated results can be extended in further creep strain analysis where a high temperature fuel element is in contact with the pressure tube at full power and high cooling conditions.

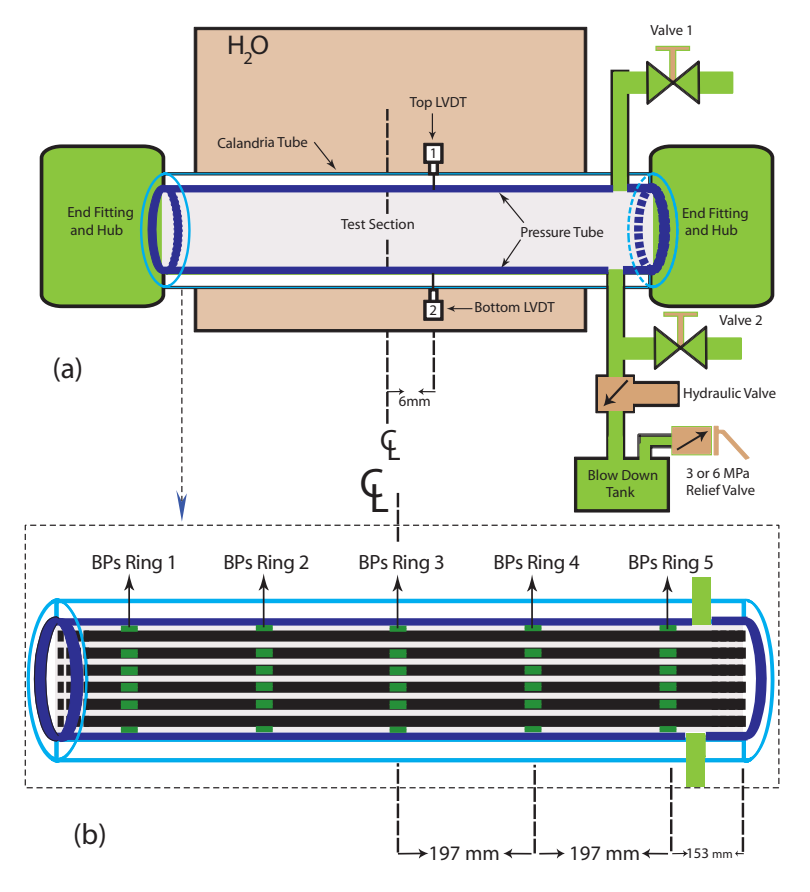


Figure 1. Schematic of the experimental apparatus (a) and Fuel channel test section (b)

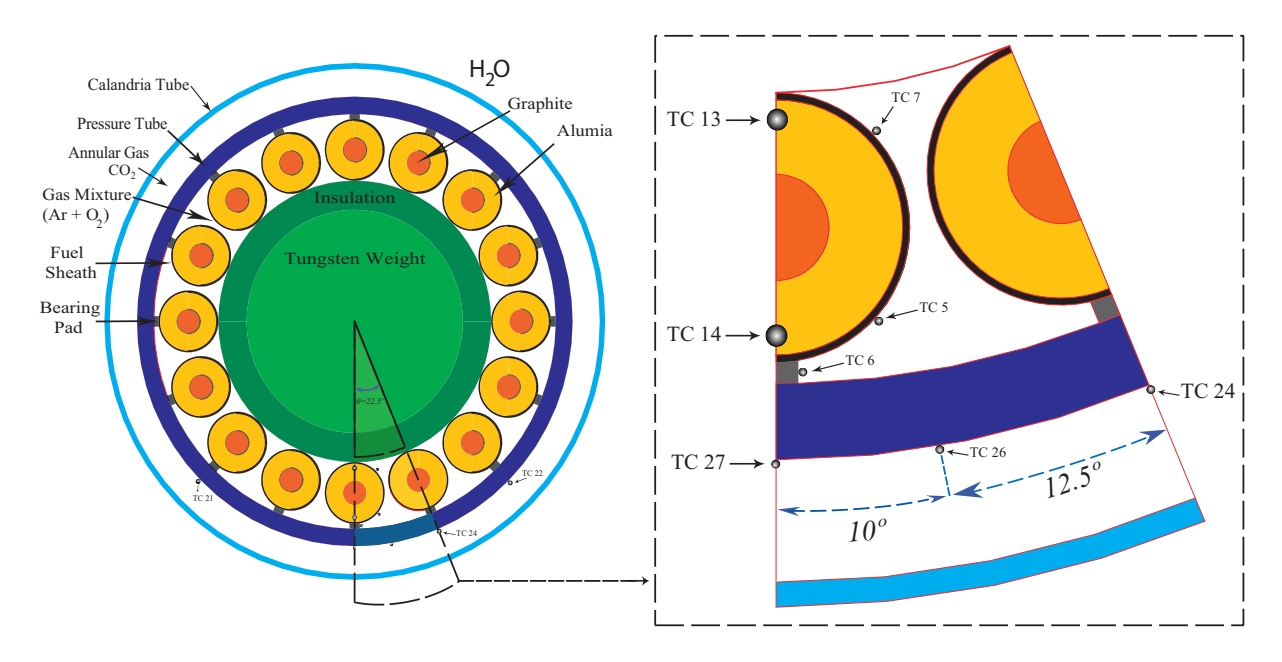


Figure 2. Fuel Element Simulator (FES) cross section located in the test section Center-Line (CL) of the BPs Ring 3.

2. EXPERIMENTAL APPARATUS, PROCEDURE AND RESULTS

According to the 28 element CANDU fuel bundle design, the apparatus made for these experiments consists of a 1.2 m long section of pressure tube mounted inside a 1.1 m long calandria tube (see Figure 1(a)). The annulus gap was purged with CO₂ and remained at atmospheric pressure throughout the experiment. The calandria tube was surrounded by a nonflowing heated water in an open tank. The top surface of the calandria tube was covered by 250 mm of water during the test. The pressure tube was connected to the blowdown tank with an opened hydraulic valve. This tank served as a reservoir to help maintain pressure during the volume change which occurs during pressure tube ballooning. Relative displacement of the pressure tube with respect to the calandria tube was monitored by top and bottom linear variable differential transformers (LVDTs) located 6 mm off the test section centreline (see Figure 1(a)). The 16 electrically heated fuel element simulators (FESs) were arranged to represent the outer ring of fuel bundle (see Figure 1(b) and Figure 2). These FESs were connected in parallel to a DC power supply. The pressure tube was pressurized with a 75% Ar and 25% O_2 gas mixture instead of steam. Each FES has an annular alumina pellet which electrically insulates the zircaloy-4 cladding from a graphite rod heater filaments. The graphite rod heater was coated with tungsten carbide to minimize the reaction between the alumina and the graphite at high temperatures.

Five axial rings of bearing and spacer pads were spot-welded to the fuel sheaths (BPs Ring 1 to 5 in Figure 1 (b)) located at the sheath axial center as well as 197 mm and 394 mm on either side of center. Each bearing pads-ring was brazed on the outermost of FESs, so that the heat transfer coupling between the fuel sheaths and these bearing pads with the pressure tube was typical of a 28 element CANDU fuel assembly (see Figure 2). Nine central tungsten weight cans were also placed inside the ring of FESs so the mass per unit length of the FES bundle (49.4 $\frac{gr}{mm}$) was similar to 28 element CANDU fuel bundles. The heated length of the test section was 1094 mm. [4]

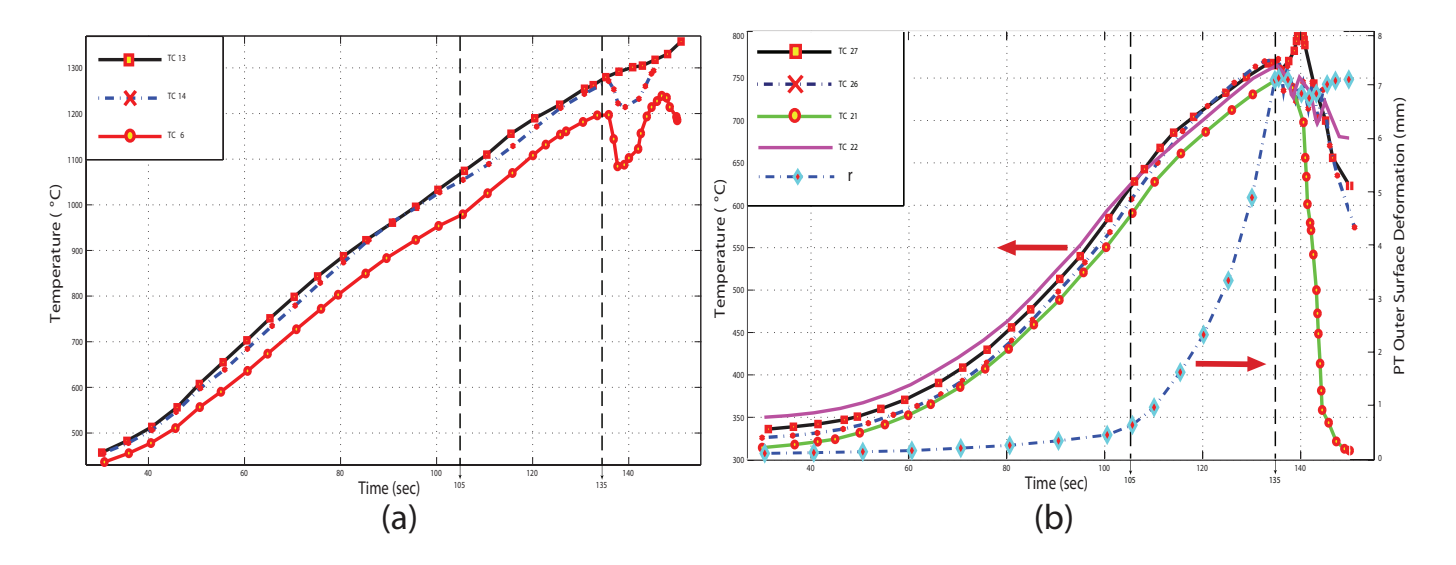


Figure 3. Thermocouple's temperatures in the bottom FES (a) and on the PT outer surface (b).

Test section temperatures were monitored with 51 thermocouples (TCs). Figure 2 shows those various thermocouples located at the FESs cross section in the test section centreline. The experiment began at a slow heatup rate in the entire FES bundle until the PT temperature approached 300° C (top to bottom PT temperature gradient was $\sim 30^{\circ}$ C). Then, the bottom seven FESs were powered at a higher power rate in 40 second where PT temperature gradient was reversed. Subsequently, the single bottom FES and bottom seven FESs were powered by alternately switching the power and power rate remained constant throughout the test. The sheath of the bottom FES was hot at the start of high power heatup, and remained hotter than the sheath temperatures on the top of the FES bundle throughout heatup phase. Figure 3 (a) shows the temperatures of TCs in the bottom FES with corresponding bearing pad temperature obtained at TC6. In fact, TC13 and TC14 were located inside the small holes in the alumina pellets in the bottom FES close to sheath inner surface. Although TC13 indicated a higher temperature than TC14 and TC6 throughout heatup phase however, heat loss to the internal tungsten weights was not disproportionately high in this experiment.

The circumferential PT temperatures at the central BP ring are shown in Figure 3 (b) where TC22 measured the highest PT temperature during heatup phase. During the ballooning phase (time interval between 105 to 135 sec) the highest temperature first occurred at TC27 when the significant PT ballooning began (~107 sec) then TC26 measured a higher temperature (120 to 135 sec) until the end of ballooning phase. The temperature profiles obtained from this experiment are therefore used as the boundary conditions for the thermal-mechanical models establish in the current study and simulation. During the heatup and ballooning phases of the fifth test, the local hot spots developed on the pressure tube under the bottom bearing pad along with the concentrated loading of the tungsten weight caused significant local PT wall thinning (~68%) under the central bottom bearing pad; whereas the circumferential wall thinning a few millimeters on either side of this bearing pad was about 20%. The wall thinning between BP rings did not show a similar deep indentation. The contact conductance between the bottom BP and PT decreased during PT straining as shown by reduction in the PT heatup rate (see TC27 temperature gradient in Figure 3 (b) during the ballooning phase). Power was decreased and the test terminated when the pressure tube to calandria tube contact occurred (t=~135 sec) and

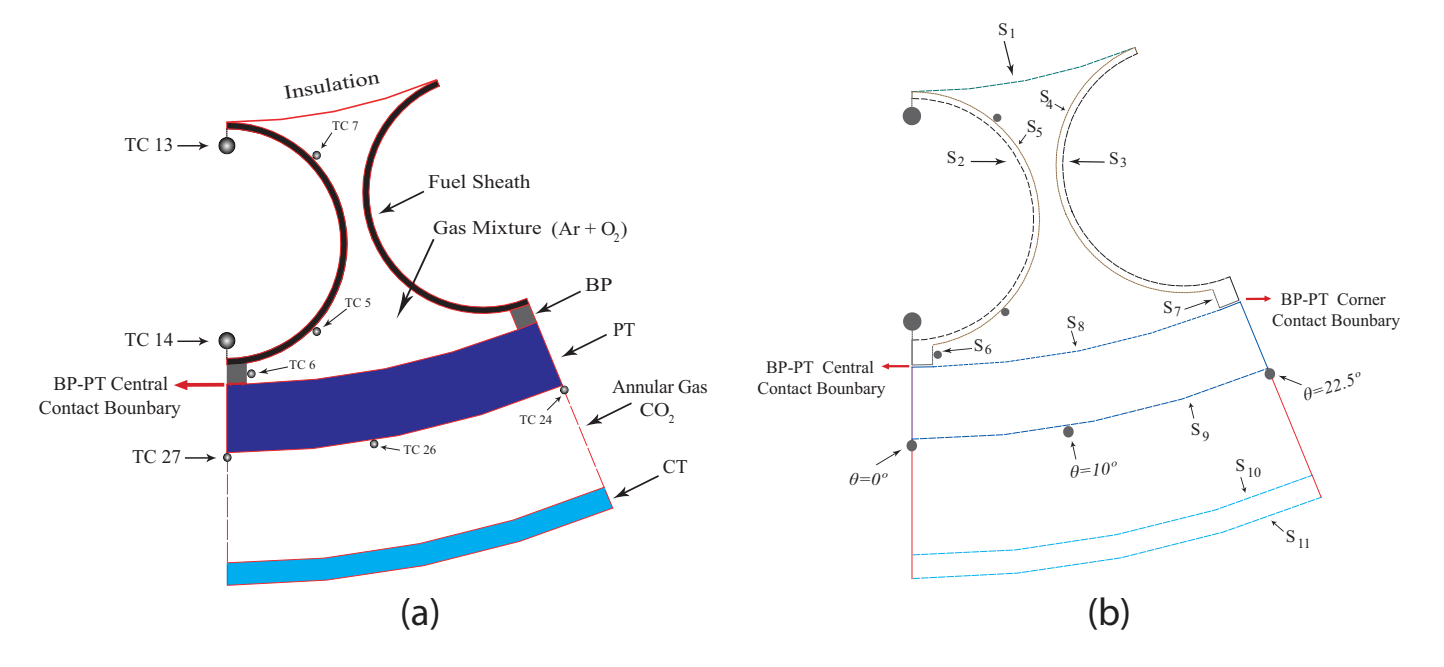


Figure 4. A 2D constructed model from the Center-Line (CL) of the BPs Ring 3 (a) and BP-PT contact boundaries of the model (b).

stable nucleate boiling was observed on the test section. The pressure tube was pressurized to 3 MPa and held constant throughout the experiment.

3. DESCRIPTION OF THE MODEL: HEAT TRANSFER

A 2D model (Figure 4 (a)) is constructed exactly similar to the fifth experimental test, in order to validate COMSOL results against this experiment and provide the bases for reliable results in further simulations. The local pressure tube creep strain deformation is the main incentive of the present study, therefore a portion of 2D cross section of the FESs located at the bottom of test section centreline will be considered (dash-line shown in Figure 2). According to the experiment, the pressure tube local thickness was drastically reduced under the central bottom bearing pad so the finite element calculations are performed to obtain pressure tube creep strain, symmetrically under these bottom bearing pads (see Figure 4 (a)). The transient heat transfer equation (1) with appropriate convective and radiation boundary conditions (equation 2,3) are considered for the fuel sheaths, the bearing pads, the pressure and calandria tubes and the transparent gas mixture regions:

$$\rho C_p \frac{\partial T}{\partial t} = \overrightarrow{\nabla} \cdot k \overrightarrow{\nabla T} + Q \qquad : \Omega$$

$$\hat{n} \cdot \overrightarrow{q''} = \overrightarrow{q_0''} + h(T_{wall} - T_{\infty}) \qquad : \partial\Omega \qquad (2)$$

$$(1 - \epsilon)R = J - \epsilon \sigma T^4 \Longrightarrow \overrightarrow{q''_{rad}} = R - J = \epsilon (R - \sigma T^4) \qquad : \partial\Omega$$
 (3)

where k(T), $C_p(T)$ and $\rho(T)$ denote respectively the thermal conductivity $(\frac{W}{mK})$, heat capacity $(\frac{J}{kgK})$ and density $(\frac{kg}{m^3})$ as a function of temperature for each domain Ω , i.e., zircaloy-4

fuel sheath and bearing pads, zirconium-2.5% niobium pressure tube, zircaloy-2 calandria tube, Ar and O_2 gas mixture and CO_2 insulation gap regions which are obtained from the ZRPRO^[6], XSteam-Matlab joint function^[7], MatWeb^[8], MATPRO^[9] and other experimental studies.^[10,11] The heat generation Q is considered zero in the all domains.

According to Figure 4 (b), the insulation boundary condition $\hat{n} \cdot \overrightarrow{q''} = 0$, has been chosen on the surface S_1 where $\overrightarrow{q''}$ is the heat flux vector and \hat{n} is the normal unit vector at boundary surface. The experimental temperature profiles obtained from TC13 and TC14 are uniformly considered on the upper and lower quadrants of the surface S_2 , respectively without consideration of any extra heat fluxes (see Figure 4 (b)) and then temperature profiles obtained on the surface S_5 and S_6 are validated with those measured at TC5, TC6 and TC7. Furthermore, only the first 40 seconds of temperature profiles obtained from TC13 and TC14 is applied on the surface S_3 in accord with the experimental conditions.

The gas mixture region is almost stagnated, therefore any motion or convection by gas is not expected. However, the radiative heat is transferred through Ar and O_2 gas mixture region and the inner surface of the pressure tube gets hotter, hence, the surface to surface radiation boundary conditions must be considered on the S_4 , S_5 , S_6 , S_7 and S_8 surfaces. With regard to radiation heat transfer, a nonparticipating transparent medium for the gas mixture region Ar and O_2 is considered that neither absorbs nor scatters the surface radiations and emits no radiation. The zircaloy emissivity is considered as $\epsilon = 0.8$ for the fuel sheath and pressure tube and σ is the Stefan-Boltzmann constant, R and S_8 , respectively are the irradiation and radiosity.

The experimental temperature profiles obtained from pressure tube outer surface i.e. TC27, TC26 and TC24 are applied on the surface S_9 with respect to the angles $\theta=0^\circ$, $\theta=10^\circ$ and $\theta=22.5^\circ$ (Figure 4 (b)). However, the temperature profiles on the azimuthal pressure tube arc length between these angles are considered to change gradually. The temperature profile at the TC24 was not reported by the authors^[4] therefore in the current simulation temperature profile at the TC24 location $\theta=22.5^\circ$ is considered as an average value of TC22 and TC27. Surface to surface radiation boundary conditions are also considered on the S_9 and S_{10} surfaces through CO₂ transparent gas. Calandria tube emissivity is considered as $\epsilon=0.2$. The S_{11} surface boundary is considered to be at fully cooled condition with the bulk temperature of surrounding water $T=74^\circ C$.^[4] The symmetry boundary conditions are also considered in both sides of the model.

4. DESCRIPTION OF THE MODEL: BP-PT CONTACT CONDUCTANCE

The BP and PT surface roughnesses prevent perfect contact from occurring when two surfaces touch each other (see BP-PT central and corner contact boundaries in Figure 4 (b)). As a result, microscopic contact and gap areas are formed. Therefore, heat is transferred through contacting boundaries of bearing pads to pressure tube by conduction through the real solid to solid microcontacts h_c , conduction through the very small interstitial gas gaps consist of argon and oxygen gas mixture h_g , and also radiation across these gas gaps h_r . If sufficient heat is transferred to the pressure tube, the local deformation of the pressure tube occurs. Therefore,

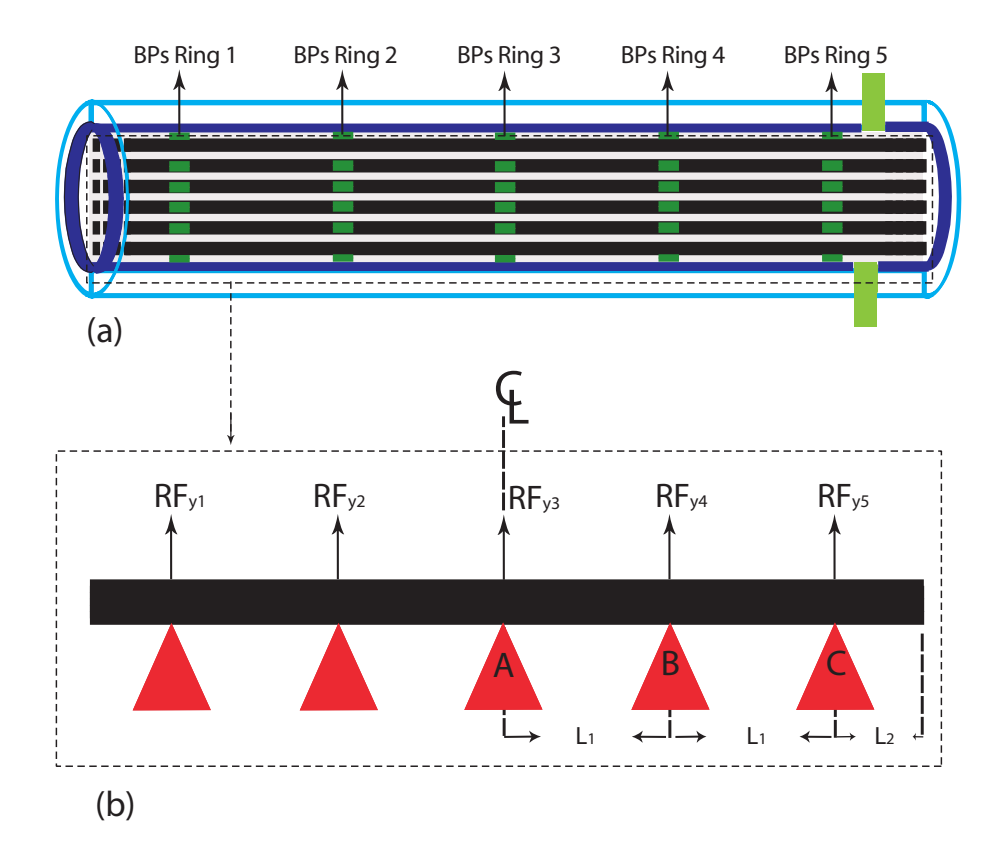


Figure 5. FES bundle (a), statically indeterminate truss (b).

the creep strain deformation of the pressure tube is directly affected by the contact conductance between the bearing pads and pressure tube and, the contact boundary dimensions (i.e., contact width and height).

A number of different contact models have been developed and published in order to obtain the total thermal contact conductance $h=h_c+h_g+h_r$ between two contacting bodies. [14] Indeed, there is no convection through each micro gas gap, therefore the conductance is modeled using the gas conductivity and a gas gap thickness is estimated based on the material roughness and mechanical load. Furthermore, the radiative heat transfer across the gap can be neglected in most applications when temperature is less than 600 °C. [13] The temperature dependent contact parameters such as thermal properties of solids and gas, gas pressure, surface curvature, surface roughness and applied load are obtained from a particular thermal-mechanical model, which can be elastic, elasto-plastic or plastic for either conforming or non-conforming contact cases. The elasto-plastic contact model. [14-18] The literature shows that the Yovanovich correlations for the plastic contact model. In the literature shows that the Yovanovich correlations for the plastic contact conductance are an improvement over older correlations and are validated for the rough surfaces of zircaloy materials such as bearing pad and pressure tube. Therefore, in the current simulation the BP-PT contact conductance transient characteristics are modeled based on Yovanovich's integral gas gap conductance h_g . [13,16]

In order to evaluate the integral gas gap, elastic and plastic contact conductances at the BP-PT central and corner contact boundaries, one needs to calculate the contact pressure imposed by BPs due to the FES bundle's weight on the inner surface of the pressure tube (see Figure 5). Based on slope deflection method, the force and moment balance equations are solved,

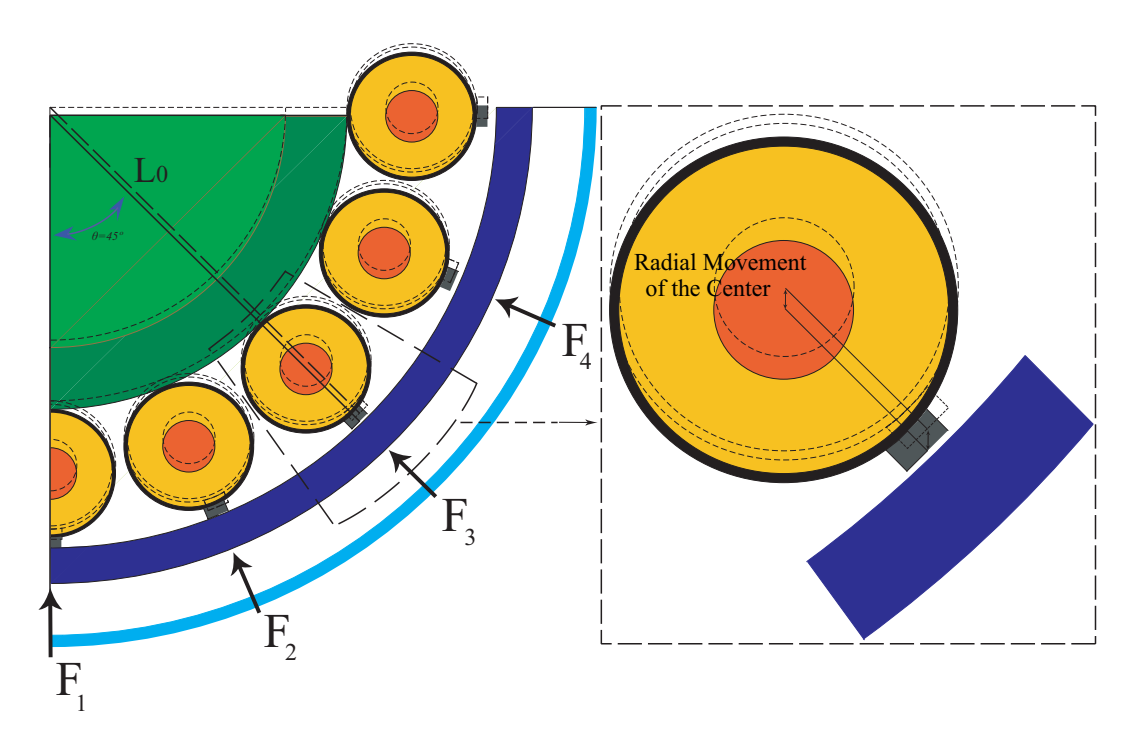


Figure 6. BPs detachment in uniform PT ballooning at t=105 s.

simultaneously. The whole FESs bundle is considered as a solid beam with an uniform mass per unit length 49.4 $\frac{gr}{mm}$ on the bottom of pressure tube where the five fixed supports (A, B, C, ...) are the representatives of the bottom BPs located in the same axial positions. Therefore, the slope deflection equations of the members AB and BC are: [19]

$$\begin{cases}
M_{AB} = 2\frac{EI}{L_1}\theta_B \\
M_{BA} = 4\frac{EI}{L_1}\theta_B \\
M_{BC} = 2\frac{EI}{L_1}(2\theta_B + \theta_C) \\
M_{CB} = 2\frac{EI}{L_1}(2\theta_C + \theta_B)
\end{cases} \implies \sum_{B,C} M = 0 \Longrightarrow \begin{cases}
RF_{y3} = 113.3 \text{ N} \\
RF_{y4} = 59.7 \text{ N} \\
RF_{y5} = 148.7 \text{ N}
\end{cases}$$

where L_1 is the length between BP rings, EI is the flexural rigidity, θ_B and θ_C are the slope angles at the support B and C, respectively and the reaction forces at each support shown by RF_y. The Euler beam simulation for the indeterminate structure using COMSOL^[5] produced the same results where the reaction force on the pressure tube inner surface in the test section centreline was 113.2 N (at the BPs Ring 3 in Figure 5 (b)). Subsequently, this load is redistributed on the seven bottom BPs of the BPs Ring 3 located in the test section centerline (see Figure 6):

$$F_1 + 2F_2 \cos 22.5^{\circ} + 2F_3 \cos 45^{\circ} + 2F_4 \cos 67.5^{\circ} = 113.2 \text{ N}$$
 (4)

where the F_1 , F_2 , F_3 and F_4 are the reaction forces imposed on the pressure tube inner's surface at the bottom bearing pad $\theta=0^\circ$ and other BP locations $\theta=22.5^\circ$, $\theta=45^\circ$ and $\theta=67.5^\circ$, respectively. In fact, the PT reaction force at the BP–PT central contact boundary imposed by fuel bundle's weight is greater than the other PT reaction forces produced at the other BP–PT locations therefore, $F_1>F_2>F_3>F_4$. [20] However, in the case of ideally equal

load distribution on the PT inner surface where $F_1 = F_2 = F_3 = F_4$, the uniform contact pressures of P=0.35 MPa is obtained at each BP-PT contact boundary. According to the fifth BP-PT experimental test, the contact pressure behavior may change especially during the ballooning phase where some of the BPs are detached from the PT inner surface at the beginning of the test in which the PT deformation is mostly uniform (see Figure 6). Therefore, the whole 113.2 N of FESs weight's load is concentrated on either the central BP-PT contact boundary where $F_2 = F_3 = F_4 = 0$ and P=1.75 MPa contact pressure is created or on the central and corner BP-PT contact boundaries in which $F_3 = F_4 = 0$ and then P=0.62 MPa contact pressure is produced, respectively. Furthermore, the local creep strain deformation of the pressure tube at the BP-PT central contact boundary could reproduce an even more complicated loading situation in which the BP-PT contact occurs again at the other BP-PT contact boundary locations.

Therefore, based on Yovanovich's correlations^[13,16] and using different zircaloy material roughnesses^[18] five contact conductance profiles are obtained on the central BP–PT contact boundary for when contact pressure is 0.35 MPa and increases step by step to its maximum value 1.75 MPa and then reduces to the first level (see Figure 7). Such a behavior could occur when the azimuthal BPs are detached from the PT inner surfaces and then reattach once local deformation is occurred on the central contact boundary. According to the Figure 7, the left-y-axis $h_{epg} = h_c^e + h_c^p + h_g$ represents the summation of elastic, plastic and gas contact conductances and the right one is the contact pressure.

It can be seen from Figure 7 that as the contact pressure and temperature are increased between the bottom BP and PT, the h_{epg} is also increases until when the local deformation is occurred at T=920 K (t = 107 sec) where the contact pressure reduces. The h_{epg} reduces momentarily, even though the pressure reduction is continued, the temperature rises and therefore the contact conductance is increased. For a roughness level of $\frac{\sigma}{m}=11.11~\mu\text{m}$, the elastic part of the contact conductance at T<730 K is calculated as $0.6 \le h_c^e(\frac{kW}{m^2K}) \le 0.8$, for T>730 K the plastic part $1.1 \le h_c^p(\frac{kW}{m^2K}) \le 58$ is obtained for the contact conductance and the gas gap conductance is calculated in the range of $7.7 \le h_g(\frac{kW}{m^2K}) \le 20.9$.

During the ballooning phase of the current simulations the contact temperature on the central contact boundary is in the range of 650 °C to 900 °C for the pressure tube and 980 °C to 1200 °C for the bearing pad (see Figure 3 (a), (b)). Therefore, based on Incropera^[12] the following correlations can be written:

$$\overrightarrow{q_{cr}''} = \frac{\sigma(T_{BP}^4 - T_{PT}^4)}{\epsilon_{BP}^{-1} + \epsilon_{PT}^{-1} - 1} \qquad \Longrightarrow \qquad h_r = \frac{\overrightarrow{q_{cr}''}}{(T_{BP} - T_{PT})} \tag{5}$$

where $\overrightarrow{q_{cr}}$ is the micro-gas gap radiation heat flux, ϵ_{BP} and ϵ_{PT} are the BP and PT emissivity, T_{BP} and T_{PT} are the BP and PT temperature in kelvin, a rough calculation of radiative heat transfer between two parallel planes with a view factor almost equal to unity, the radiation conductance is calculated in the range of 0.2 to 0.35 $\frac{kW}{m^2K}$.

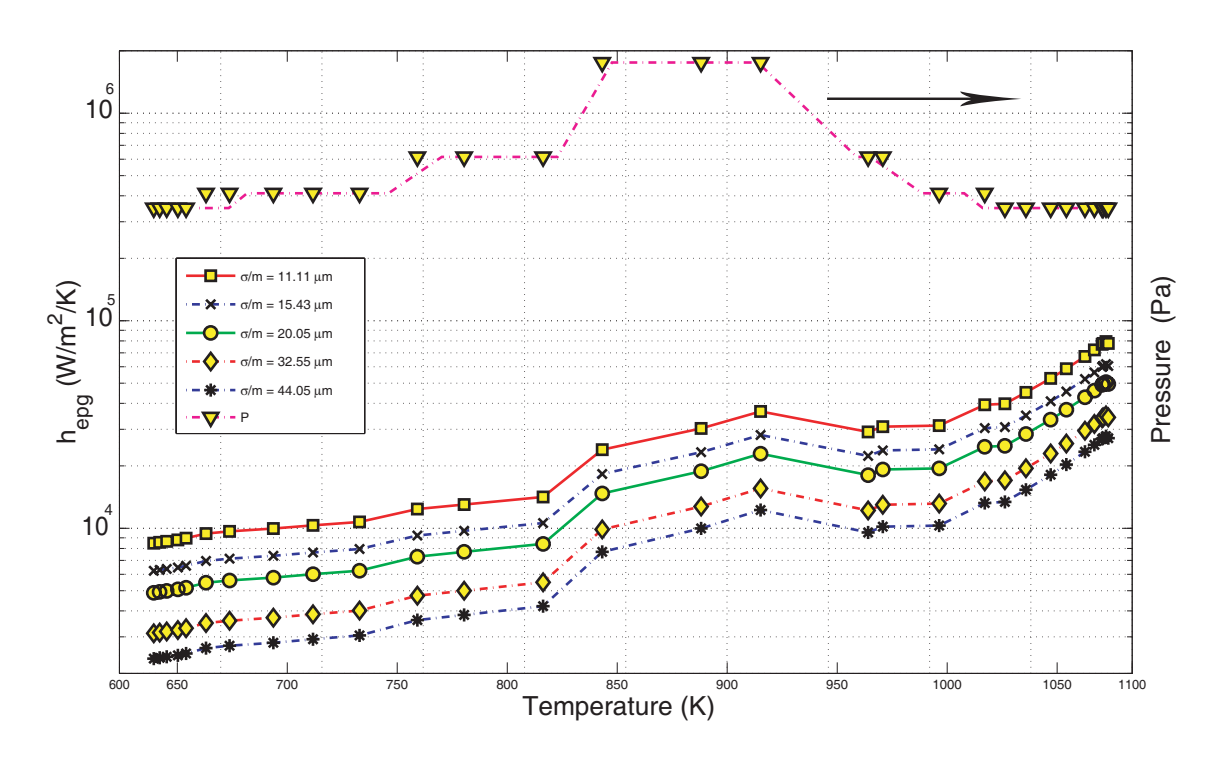


Figure 7. Pressure profile and contact conductance for different material roughness.

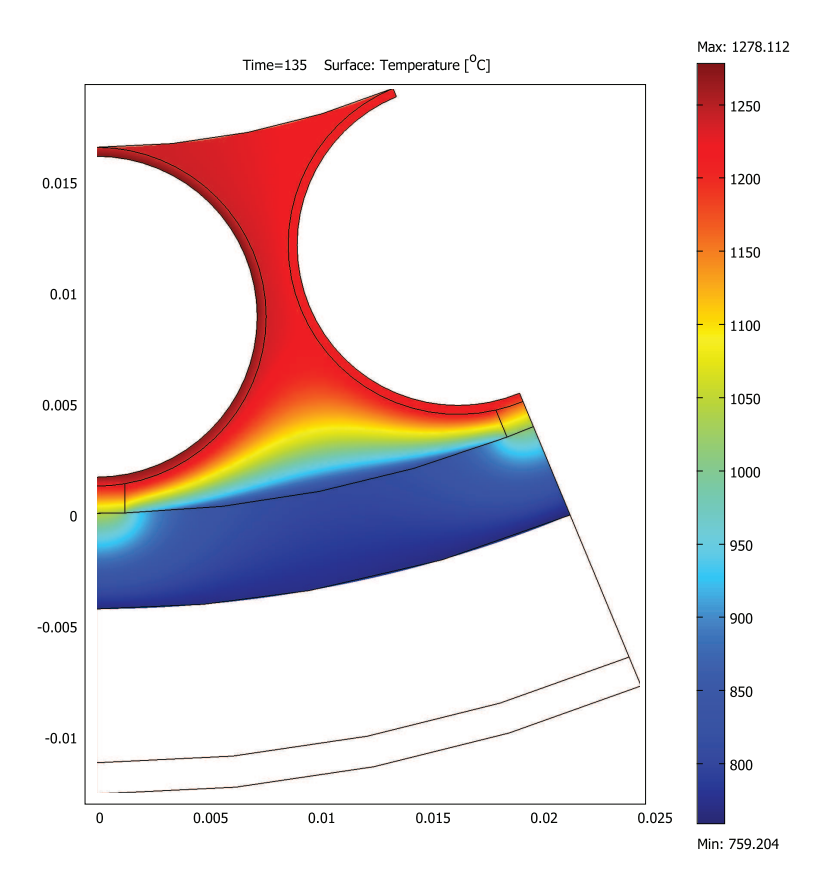


Figure 8. Temperature profile of the domain at t=135 s.

5. HEAT TRANSFER WITH BP-PT CONTACT CONDUCTANCE RESULTS:

Figure 8 shows the solution to the energy equation for the BP-PT contact model at $t=135~\rm s$ and for a roughness level of $\frac{\sigma}{m}=11.11~\mu \rm m$. According to the contact pressure obtained in this simulation (see Figure 7), the total contact conductances calculated from previous section are imposed in both BP-PT central and corner contact boundaries (Figure 4 (b)) and PT temperature profile is obtained. A sensitivity analysis is performed on the emissivity of the pressure tube inner surface and the FES's sheaths in order to obtain the same temperature according to the TC5 and TC6 of the experiment (see Figure 2). As the temperature between the bottom BP and PT increases, the PT thickness temperature under the bottom BP rises to the values higher than 650 °C where zircaloy creep strain is significantly increased due to α to β phase change. The maximum temperature is obtained in the FES's sheath domain while the pressure tube maximum temperature is found to be at the BP-PT contact boundaries. This is because of the fact that heat generated in the graphite pellet could properly transfer into the zirconium sheath by conduction but partially conducted to the PT through contact width and then transferred through PT thickness to the annulus gas gap. The behavior of temperature profile obtained for pressure tube at each time step are pretty similar to that of $t=135~\rm s$.

6. DESCRIPTION OF THE MODEL: STRUCTURAL MECHANICS AND CREEP STRAIN

The local deformation of the pressure tube occurs as a consequence of localized hot spots which will produce in the region of contact (see BP-PT central and corner contact boundaries in Figure 4 (b)), if sufficient heat is transferred to the pressure tube through conduction and radiation. Therefore, the creep strain deformation of the pressure tube is directly affected by the contact conductance between the BPs and PT and by the FESs radiation to the PT inner surface. According to the experiment, the pressure tube is under combined internal pressure and radialcircumferential temperature gradient, hence the hot spot created by bottom BP contact resulted in PT wall thinning directly under the bottom bearing pad. Therefore, the stress-strain equation 5.1.4 from Mendelson^[21] are solved for the pressure tube in the 2D cross section of test section centreline (see Figure 4 (a)). In fact, we have assumed that a state of plain strain $e_z = 0$ is produced where the axial length of pressure tube is very large compare to the width of loaded region. Therefore, the strain tensor components are only defined in the two dimensional cases. Understanding creep strain in zircaloy materials such as pressure tube used in CANDU reactors is very important especially at higher temperatures. This was accomplished by Shewfelt et al., [22,23] where both transverse and longitudinal samples from actual CANDU pressure tubes were examined in a uniaxial creep test apparatus. The tests were successful in predicting the creep strain over a wide range of temperature ramp rates of 1 to 50 $\frac{{}^{\circ}C}{sec}$, the stress range of 5 to 100 MPa. There were also successful in predicting the transverse creep of a section of internally pressurized tube which was heated at about 5 $\frac{{}^{\circ}C}{sec}$, over a range of internal pressures from 0.5 to 10 MPa. These tests cover all the conditions that could occur in a CANDU pressure tube during a postulated loss of coolant accident (LOCA). The authors concluded that the zircaloy creep strain is significantly increased at temperatures greater than approximately 650 °C due to α to β phase change. Shewfelt developed creep strain rate for the zirconium-2.5% niobium pressure tube in two separate temperature ranges. These equations however are used in order to drive a mathematical creep model for the pressure tube under multiaxial stress condition:^[21]

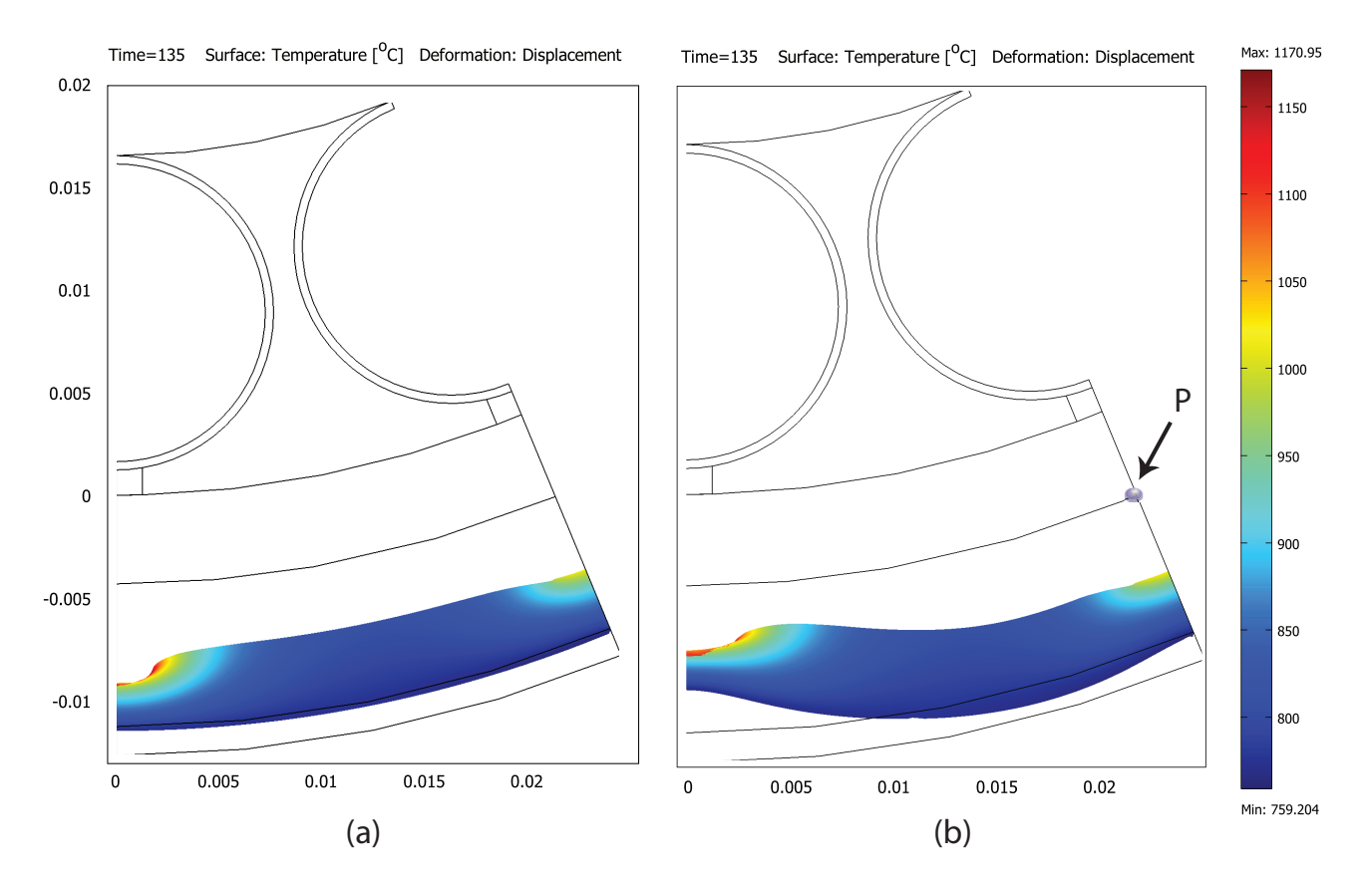


Figure 9. PT deformation profile at t=135 s (a) uniform LVDT (b) single point LVDT.

$$\dot{e}_{ij}^{c} = \frac{3}{2} \frac{S_{ij}^{d}}{\sigma_{e}} \dot{e}^{c} \qquad \text{where:} \qquad \begin{cases} S_{x}^{d} = \frac{2S_{x} - S_{y} - S_{z}}{3} \\ S_{y}^{d} = \frac{2S_{y} - S_{z} - S_{x}}{3} \\ S_{z}^{d} = \frac{2S_{z} - S_{x} - S_{y}}{3} \end{cases}$$
(6)

where \dot{e}_{ij}^c is the strain tensor, S_{ij}^d is the stress deviator tensor and S_x^d , S_y^d and S_z^d are the stress deviator components in the x, y and z direction of the Cartesian coordinate system.

7. PRESSURE TUBE CREEP STRAIN DEFORMATION RESULTS:

The pressure tube is under combined internal pressure and radial-circumferential temperature gradient, therefore a nonuniform temperature profile obtained from preceding equations is used to calculate pressure tube creep strain deformation and wall thinning under bottom BP–PT contact. Two set of boundary condition are used on the PT outer surfaces in order to follow the PT bulk deformation (see Figure 9). It can be seen in Figure 9 (a) when uniform LVDT results is used on the PT outer surface a wall thinning of 47% is obtained however when single point LVDT results is imposed only at P point of PT outer surface 58% of wall thinning is obtained. The rest of PT boundaries are considered to be free. According to experiment, during the high power heatup phase and contact ballooning, significant preferential wall thinning (~68%) occurs directly under the bottom bearing pad. The results obtained here are very close to those measured at the fifth experiment, therefore we could extend our validation for the next step of simulation where fuel element to pressure tube contact occurred under full power and high cooling condition.

8. CONCLUSION

Thermal-mechanical behavior of the bearing pad to pressure tube contact is considered here in order to investigate potential challenges in fuel channel integrity. We have attempted to simulate several analytical contact models which are the solutions to the transient heat transfer, thermal-mechanical and creep strain equations along with appropriate boundary conditions as a validation analysis for the creep strain calculations of the CANDU fuel element to pressure tube contact. The results described here quantify the conditions under which BP–PT contact cases could create localized high temperature on the inner surface of a pressure tube where the pressure tube local strain is occurred. Two different set of simulations have been performed based on LVDT boundary consideration. The value of parameters considered in these simulations cover a very broad range and in many cases. However, the most sensitive parameters which significantly affecting the contact modelling are i.e., the emissivity ϵ , contact conductance h and contact width L_c . The results demonstrate the strong sensitivity of maximum pressure tube temperature and local strain to the contact conditions and indicate that any local pressure tube deformation will act to reduce the heat transfer to the pressure tube and therefore, will be self-limiting.

ACKNOWLEDGMENTS

Financial support from the Natural Sciences and Engineering Research Council of Canada (NSERC) and the University Network of Excellence in Nuclear Engineering (UNENE) is gratefully acknowledged.

REFERENCES

- 1. Moyer, R.G. and Sanderson, D.B. and Tiede, R.W. and Rosinger, H.E., "Bearing-Pad/Pressure-Tube Rupture Experiments", *Proc.* 13th CNS Annual Conf., p 156-62, (1992).
- 2. M.H. Bayoumi, W.C. Muir, P.B. Middleton, "Simulation and Analysis of Bearing Pad to Pressure Tube Contact Heat Transfer under Large Break LOCA Conditions", *Proc.* 17th *CNS Annual Conf.*, Toronto, (1996).
- 3. Moyer, R.G. and Gillespie, G.E., "Pressure-Tube/Calandria-Tube Contact Heat Transfer Experimental Data", *CANDEV-86-95 Atomic Energy of Canada Limited*, Whiteshell Laboratories, (1986).
- 4. Moyer, R.G. and Sanderson, D.B. and Demoline, K.W., "Bearing-Pad/Pressure-Tube Rupture Experimental Summary Report for Series Tests 5-12", *COG-94-252 Atomic Energy of Canada Limited*, *Whiteshell Laboratories*, (1994).
- 5. COMSOL Heat Transfer Module User's Guide, http://www.comsol.com, (2010).
- 6. K.R. Mayoh, "A Compendium of Material Properties for Zirconium Alloys", COG-96-101, (1997).
- 7. M. Holmgren, "XSteam for MATLAB, Thermodynamic Properties of Water and Steam", http://www.mathworks.com, (2007).

- 8. MatWeb, "MatWeb, Material Property Data", http://www.matweb.com, (2010).
- 9. SCDAP/RELAP5, "CODE MANUAL VOLUME IV: MATPRO A LIBRARY OF MATERIALS PROPERTIES FOR LIGHTWATER REACTOR ACCIDENT ANALYSIS", *Idaho National Engineering and Environmental Laboratory*, MOD3.2, (1997).
- 10. Tiesinga, B. W. and Sakonidou, E. P. and Van den Berg, H. R. and Luettmer Strathmann, J. and Sengers, J. V., "The Thermal Conductivity of Argon in the Critical Region", *Journal of Chemical Physics*, v 101, n 8, p 6944-6963, (1994).
- 11. Dordain, L. and Coxam, J. and Quint, J. and Grolier, J. and Lemmon, E. and Penoncello, S., "Isobaric heat capacities of carbon dioxide and argon between 323 and 423 K and at pressures up to 25 MPa", *The Journal of Supercritical Fluids*, v 8, n 3, p 228-235, (1995).
- 12. F. Incropera, D. DeWitt, "Introduction to Heat Transfer", second edition, (1990).
- 13. M.M. Yovanovich, "Micro and Macro Hardness Measurements, Correlations, and Contact Models", *Collection of Technical Papers 44th AIAA Aerospace Sciences Meeting*, v 16, p 11702-11729, (2006).
- 14. Sridhar, M. R. and Yovanovich, M. M., "Review of Elastic and Plastic Contact Conductance Models: Comparison with Experiment", *Journal of Thermophysics and Heat Transfer*, v 8, n 4, p 633-640, (1994).
- 15. Mikic, B. B., "Thermal Contact Conductance: Theoretical Considerations", *International Journal of Heat and Mass Transfer*, v 17, n 1, p 205-214, (1974).
- 16. Song, S. and Yovanovich, M. M. and Nho, K., "Thermal Gap Conductance: Effects of Gas Pressure and Mechanical Load", *Journal of Thermophysics and Heat Transfer*, v 6, n 1, p 62-68, (1992).
- 17. Ross, A. M. and Stoute, R. L., "Heat Transfer Coefficient Between Uranium Dioxide and Zircaloy-2", *Atomic Energy of Canada Limited, Whiteshell Laboratories*, n 1552, (1962).
- 18. Hegazy, A. A., "Thermal Joint Conductance of Conforming Rough Surfaces: Effect of Surface Microhardness Variation", *University of Waterloo*, Ph.D thesis, (1985).
- 19. McCormac, J. C. and Nelson, J. K., "Structural Analysis: A Classical and Matrix Approach", *John Wiley and Sons*, New York, (1997).
- 20. Lazovic, T. and Ristivojevic, M. and Mitrovic, R., "Mathematical Model of Load Distribution in Rolling Bearing", *FME Transactions*, v 36, n 4, p 189-196, (2008).
- 21. A. Mendelson, "Plasticity: Theory and Application", Macmillan, New York, (1968).
- 22. R.S.W. Shewfelt, L.W. Lyall, D.P. Godin, "A High-Temperature Creep Model for Zr-2.5 wt% Nb Pressure Tubes", *Journal of Nuclear Materials*, v 125, i 2, p 228-235, (1984).
- 23. R.S.W. Shewfelt, L.W. Lyall, "A High-Temperature Longitudinal Strain Rate Equation for Zr-2.5 wt% Nb Pressure Tubes", *Journal of Nuclear Materials*, v 132, i 1, p 41-46, (1985).